Nuclear Materials and Energy 19 (2019) 516–523

Contents lists available at ScienceDirect

Nuclear Materials and Energy

journal homepage: www.elsevier.com/locate/nme

Optimization of the snowflake divertor for power and particle exhaust on NSTX–U

P.J. Vail*, O. Izacard, E. Kolemen*

Department of Mechanical and Aerospace Engineering, Princeton University, Princeton, New Jersey, USA

ARTICLE INFO

Keywords:
NSTX-U
snowflake divertor
cryopump
UEDGE

ABSTRACT

In this paper, simple analytical modeling and numerical simulations performed with the multi-fluid edge transport code UEDGE are used to identify optimal snowflake divertor (SFD) configurations for heat flux mitigation and sufficient cryopumping performance on the National Spherical Torus eXperiment Upgrade (NSTX–U). A model is presented that describes the partitioning of sheath-limited SOL power and particle exhaust in the SFD as a result of diffusive transport to multiple activated strike points. The model is validated against UEDGE predictions and used to analyze a database of 70 SFD-minus equilibria. The optimal location for the entrance to a divertor cryopumping system on NSTX–U is computed for enabling sufficient pumping performance with acceptable power loading in a variety of SFD-minus configurations. UEDGE simulations of one promising equilibrium from the database indicate that a significant redistribution of power to the divertor legs occurs as a result of neutral particle removal near one of the SFD-minus strike points in the outboard scrape-off layer. It is concluded that pump placement at the optimal location is advantageous as the large number of compatible equilibria reduces the precision required of real-time SFD configuration control systems and enables acceptable divertor solutions even if UEDGE-predicted power redistribution slightly reduces the achievable pumping performance.

1. Introduction

The National Spherical Torus eXperiment Upgrade (NSTX–U) [1], which completed its first campaign of plasma operations in 2016 [2,3], is a spherical tokamak (ST) at the Princeton Plasma Physics Laboratory (PPPL) that has been commissioned to build upon the successes of previous STs such as NSTX [4] and the Mega-Ampere Spherical Tokamak (MAST) [5] and to establish the scientific baseline required for the design of future ST-based fusion facilities. NSTX–U received substantial hardware improvements to enable plasma operations at 1 T, 2 MA, 10 MW and discharge durations of up to 5 s. These enhancements will afford access to new physics regimes for the investigation of matters such as the dependence of energy confinement on electron collisionality [6], the physics of energetic ions [7], and the development of fully non-inductive scenarios at high pressure and current [8].

A combination of technologies will be required on NSTX–U for enabling reliable access to high-performance scenarios while ensuring acceptable margins on device safety. Of particular importance will be strategies that address the management of power and particle exhaust at the plasma-material interface (PMI). One of the most challenging issues for NSTX–U will be the mitigation of reactor-level power fluxes onto plasma-facing components. It was shown in [1] that the peak axisymmetric heat flux cannot exceed 10 MW/m^2 without risking structural damage to the graphite divertor tiles, and this requirement may become more demanding as the impact of toroidally-asymmetric heat loads (due to non-axisymmetric fields and tile misalignments) on divertor tile performance is analyzed during the NSTX–U recovery project. NSTX–U will also require robust control of main ion and impurity densities to access regimes of reduced collisionality, sustain non-inductively driven plasma currents, and avoid the tokamak density limit [9]. The power and particle exhaust challenge is further complicated by the highly-localized PMI, resulting from the compact device size and the extremely narrow scrape-off layer (SOL) width at high plasma current (3 mm at 2 MA) [10]. The dual challenges of power and particle exhaust therefore necessitate the development of integrated PMI solutions that enable efficient and simultaneous control of these quantities.

One of the most promising heat flux mitigation strategies that is being considered for NSTX–U is the use of an advanced magnetic configuration known as the snowflake divertor (SFD) [11]. Unlike the magnetic topology of the conventional single-null (SN) divertor, the field of the exact SFD configuration is characterized by a second-order null on the primary separatrix that forms a hexagonal structure

* Corresponding authors.
E-mail addresses: pjv@princeton.edu (P.J. Vail), ekolemen@princeton.edu (E. Kolemen).

https://doi.org/10.1016/j.nme.2019.03.003
Received 15 August 2018; Received in revised form 3 February 2019; Accepted 2 March 2019
Available online 19 April 2019

reminiscent of a snowflake. In practice, one of two alternative magnetic topologies is obtained: (1) the SFD-plus with a secondary X-point in the private flux region, and (2) the SFD-minus in which the secondary X-point lies in the SOL. These configurations have several properties that are advantageous for heat flux reduction, including high poloidal flux expansion leading to a larger plasma-wetted area, a longer average SOL connection length that promotes increased radiative losses, and the existence of additional strike points (SPs) across which the power flux may be shared.

In addition to TCV [12–16], DIII–D [17], and EAST [18], NSTX was one of the first devices to perform experimental studies of the SFD configuration [19,20]. Equilibrium reconstructions of 1 MA, 0.5 T, 5 MW neutral beam-heated discharges indicated that the poloidal flux expansion in the SFD was nearly four times higher than that in the SN divertor with a corresponding twofold increase in the connection length for the 1.5 mm (at the midplane) flux tube adjacent to the separatrix. The existence of these magnetic properties coincided with a fivefold decrease in the peak heat flux (from 5 to 1 MW/m^2) for the discharges reported in [20]. Furthermore, it was observed that the SFD caused no degradation of core and pedestal performance, as characterized by plasma parameters such as β_N, stored energy, and H-mode confinement time. Recent work has focused on developing candidate SFD scenarios and predicting divertor performance for NSTX–U through a combination of free-boundary equilibria design and edge plasma simulations. In [21], it was shown that a variety of snowflake configurations can be generated with the up-down symmetric divertor coils on NSTX–U across a range of plasma currents and Ohmic fluxes and without exceeding limits on the allowable coil currents. Furthermore, modeling with the multi-fluid edge transport code UEDGE [22] has indicated, for instance, that large flux expansion SN divertors closer to the SFD undergo a more gradual transition to full detachment with a detachment threshold at lower core density than in the conventional SN divertor [23,24].

While the mitigation of power exhaust requires the use of novel PMI solutions such as the SFD, control of main ion and impurity densities on NSTX–U will likely be accomplished with more conventional techniques. In particular, hardware upgrades may include the installation of a divertor cryopumping system, which is a technology that has been employed for density control on several devices [25,26]. An initial physics-based design of a cryopumping system for NSTX–U recently demonstrated the feasibility of pumping the 10 MW (20 Torr-L/s) neutral beam-heated scenario in a SN configuration with a pump plenum and baffling structure located in the lower outboard divertor [27]. A semi-analytical first-flight neutral transport model [28], corrected to include the effects of neutral particle conductance through a long duct as computed by the Monte Carlo neutral transport code EIRENE [29], was used along with exponential profiles of divertor heat and particle fluxes to determine candidate pump locations and required plenum dimensions for target pump inlet pressures. Simulations of the cryopump design were performed with the two-fluid plasma and kinetic neutral code SOLPS [30] to analyze pump performance in standard and large flux expansion SN equilibria for a range of core and divertor parameters, including in conditions of near-detachment. Simulation of cryopumping performance in the SFD using SOL transport codes remains an outstanding research task.

Experimental results from NSTX and design studies for the device upgrade strongly suggest that the SFD configuration, in conjunction with a divertor cryopumping system, may provide an attractive solution to the combined challenges of power and particle exhaust management on NSTX–U. Preliminary analyses have indicated that large flux expansion divertors may improve pumping performance due to radial translation of SOL fieldlines toward the pump entrance [23,27]. However, while affording considerable insight into the compatibility of alternative divertor configurations with a cryopumping system, these studies only considered a small number of large flux expansion SN equilibria with secondary X-points located close to, but not inside, the limiter surface.

This prior work has been limited in scope due to several factors: While standard analytical models, such as the commonly-used transport model for SN divertors as derived in [31], may be assumed to adequately describe the divertor profiles in large flux expansion SN equilibria, a generalized model of power and particle fluxes is required for the analysis of arbitrary SFD configurations to account for diffusive transport and the partitioning of fluxes among multiple SPs. A model that is tailored to the unique characteristics of the SFD may be used to determine the dependencies of power and particle exhaust on magnetic topology and may enable the identification of optimal SFDs for heat flux mitigation and pumping performance. These optimal configurations may then be employed, for instance, as targets in real-time feedback control algorithms [32,33]. Recent work on TCV and ASDEX Upgrade has suggested one approach to the extension of existing models to the SFD [16,34]. Prior analyses with SOL transport codes have also been limited by the challenge of constructing computational grids for equilibria that contain multiple X-points in the solution domain. Only within the last few years has the development of advanced grid generation capabilities enabled the simulation of a broader variety of equilibria (including SFDs) in EMC3-EIRENE [35], UEDGE [36,37], and SOLPS [38].

In this paper, we employ simple analytical modeling and UEDGE numerical simulations to identify optimal SFD configurations for heat flux mitigation and cryopumping performance on NSTX–U. In Section 2, we describe a generalized analytical model that was developed to predict the sheath-limited divertor profiles of power and particle exhaust in the SFD. In Section 3, we use the model to analyze an equilibria database and to assess the impact of SFD magnetic geometry and cryopump positioning on divertor power exhaust and pumping performance. One of the most promising equilibria is selected and used, in Section 4, as the basis for a more detailed analysis of divertor performance with UEDGE. Finally, in Section 5, we summarize our results and discuss plans for future work.

2. SFD power and particle flux model

In this section, we present a simple analytical model that has been developed for estimating the sheath-limited divertor profiles of power and particle flux in the SFD on NSTX–U. The proposed model generalizes the standard divertor model of [31] by allowing for SOL flux surfaces of varying connection length, thereby enabling the study of divertor transport in the presence of large connection length gradients (as often exist between the primary and secondary separatrices in the SFD-minus). Rather than assuming a fixed functional form for the SFD target profiles (as is done in [16,34]), the proposed model explicitly evolves the parallel heat flux from divertor entrance to target by first solving a one-dimensional diffusion problem for each flux tube. The model will be used in Section 3 to study a database of SFD equilibria. The required inputs to the model are the poloidal flux map from a Grad–Shafranov equilibrium calculation, a specification of the poloidal contour of the limiting surface, and several scalar parameters defining the power balance and transport properties in the SOL. Model predictions for several representative SFDs from the equilibria database of Section 3 are presented. In addition, we show that the profiles as predicted by the simple model are in good qualitative agreement with those computed by UEDGE. In this paper, we confine our analysis to profiles on the low-field-side (outboard) divertor, which is the most suitable location for the installation of a cryopumping system on NSTX–U.

2.1. Power flux model

Similar to the model used for standard divertors [31], the analytical model for the SFD only attempts to describe SOL transport in the region from the divertor entrance to the divertor target. To accurately define the divertor entrance in SFD-minus configurations, however, the

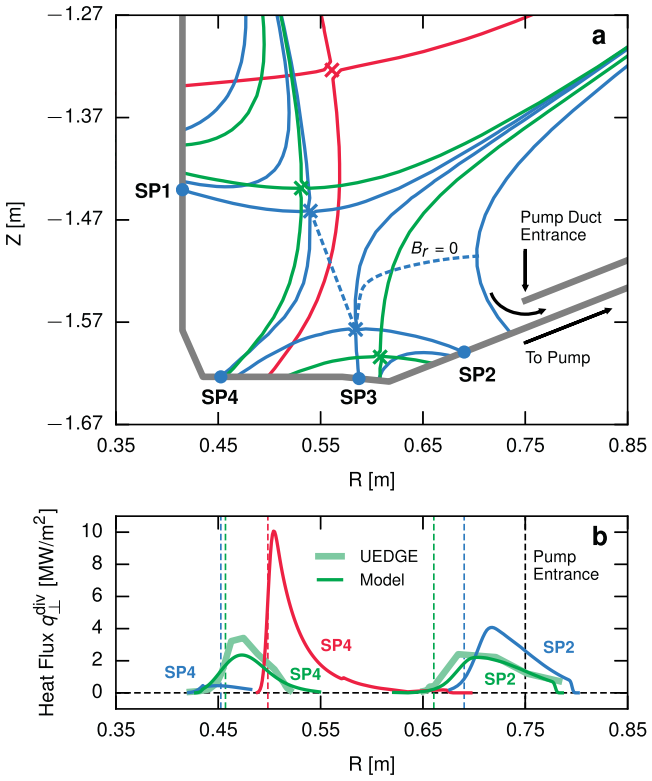

Fig. 1. Heat flux profiles (b) as computed by the simplified analytical model for three representative divertor configurations on NSTX–U, as shown in (a): large flux expansion single-null (red) as well as SFD-minus with large distance between X-points (green) and reduced distance between X-points (blue). Also shown in (b) are the UEDGE predicted profiles for the green SFD-minus equilibrium. In (a), the labels SPi for $i \in \{1, 2, 3, 4\}$ denote the four strike points of the blue SFD-minus equilibrium. Also shown in (a) and (b) is the approximate location of the entrance to the divertor cryopump which is used for pump performance analysis in Section 3. (For interpretation of the references to color in this figure legend, the reader is referred to the web version of this article.)

standard model must be modified to address the complexities which result from the presence of a secondary separatrix in the SOL. For this purpose, we introduce a construct which we refer to as the splitting front, defined as the union of two curves: (1) the line joining the X-points, and (2) the contour along which the radial component of the magnetic field $B_r = 0$ extending from the secondary X-point to the outboard SOL. We provide an illustration of the splitting front for a representative SFD-minus equilibrium in Fig. 1(a) (blue dashes). The splitting front should, strictly speaking, be defined by the curves which are perpendicular to the flux surfaces in these regions. It was determined by visual inspection that the line joining the X-points and the curve $B_r = 0$ provide reasonable approximations to the perpendicular curves without requiring detailed integration across flux surfaces. The choice was therefore made to define the splitting front using the X-point line and the $B_r = 0$ curve due to the computational simplicity of this approach. It is observed in Fig. 1 that the SOL is divided into two largely independent domains extending from the splitting front (which we will consider to be the divertor entrance) to the strike points SP2 and SP4, respectively. This magnetic topology therefore suggests that the power flux analysis for the SFD-minus should be performed in two independent domains which extend from the splitting front to the two active strike points.

To define the initial heat flux profile at the splitting front, we begin with the standard assumption that the parallel heat flux in the SOL at the plasma midplane assumes an exponentially-decaying profile with characteristic length scale $\lambda_q = 3$ mm, the expected value for NSTX–U at 2 MA [10]. The peak parallel heat flux at the midplane is then computed as,

$$q_{\parallel}^{\mathrm{mid,peak}} = \frac{P_{\mathrm{heat}}(1 - f_{\mathrm{rad}})f_{\mathrm{OBD}}}{4\pi R_{\mathrm{mid}}\lambda_q (B_\theta/B)_{\mathrm{mid}}}, \tag{1}$$

where P_{heat} is the total input heating power (Ohmic + auxiliary), f_{rad} is the radiated power fraction, f_{OBD} is the fraction of SOL power which flows to the outboard divertor, R_{mid} is the major radius at the outer midplane, and B_θ and B are the poloidal and total magnetic field strengths, respectively, both of which are evaluated at the plasma midplane. In this paper, we select $P_{\mathrm{heat}} = 10$ MW, which is the expected maximum beam power for NSTX–U, $f_{\mathrm{rad}} = 0.2$, and $f_{\mathrm{OBD}} = 0.7$, both of which are projections for NSTX–U based upon experimental results from NSTX. Furthermore, for all equilibria, $R_{\mathrm{mid}} = 1.5$ m $\pm$ 0.5 mm. After defining the heat flux profile at the outer midplane, we partition the SOL into a set of magnetic flux surfaces extending from major radius $R = R_{\mathrm{mid}}$ to $R = R_{\mathrm{mid}} + 3\lambda_q$. The exponentially-decaying profile at the outer midplane is then projected along flux surfaces to the splitting front for use as the initial condition of the SFD-minus power flux analysis.

For the ith flux surface ψ_i, we model the time-evolution of the parallel heat flux as a one-dimensional heat diffusion problem with initial condition defined by a rectangular function of magnitude $q_{\parallel i}^{\mathrm{split}}$ and width $\Delta\psi_i$, where $q_{\parallel i}^{\mathrm{split}}$ is the parallel heat flux on the surface at the splitting front and the width $\Delta\psi_i$ is the flux difference between adjacent surfaces ψ_i and ψ_{i+1}. As the flux surface is traversed from splitting front to divertor target, the parallel heat flux diffuses across fieldlines onto neighboring flux surfaces. The total divertor heat flux profile is then computed as the summation of the individual diffused profiles along the target. For a flux surface ψ_i, the diffused profile distributed across arbitrary flux surfaces ψ at an arbitrary time t is given by the convolution of the initial condition with the expression,

$$\Phi(\psi, t) = \frac{1}{2\sqrt{\pi\chi t}} \exp\left(-\frac{\psi^2}{4\chi t}\right), \tag{2}$$

where χ is the thermal diffusivity in units of Wb^{2}s^{-1}. We note that the use of a diffusion coefficient with dimensions of squared-flux per time assumes that there will exist a strong enhancement of diffusive transport in the region of low poloidal field. We computed $\chi = 5 \times 10^{-3}$ Wb^{2}s^{-1} by fitting the Eich divertor profile [39] to a UEDGE-computed heat flux profile at SP2 and then extracting χ from the profile fit parameters. To compute $q_{\parallel i}^{\mathrm{div}}$, the parallel heat flux profile at the divertor target due to the flux surface ψ_i, we set $t = t_{\mathrm{TOF}} = L_\parallel/c_s$, the time-of-flight (TOF) on the fieldline, where $L_\parallel$ is the parallel connection length for the fieldline from splitting front to target and c_s is the sound speed. Finally, the perpendicular heat flux on the divertor where θ_B is the angle-of-incidence on the divertor target for the given fieldline.

In Fig. 1(b), we depict the perpendicular heat flux profiles as computed by the simplified analytical model for three representative equilibria: (1) a large flux expansion SN (red) with $\psi_{N,2} = 1.052$, (2) a SFD-minus of large X-point separation distance (green) with $\psi_{N,2} = 1.008$, and (3) a SFD-minus of reduced X-point separation distance (blue) with $\psi_{N,2} = 1.002$. For each equilibrium, $\psi_{N,2}$ is the normalized flux of the secondary separatrix and is computed as $\psi_{N,2} = (\psi_{X,2} - \psi_M)/(\psi_{X,1} - \psi_M)$, where $\psi_{X,2}$, ψ_M, and $\psi_{X,1}$ are the magnetic fluxes of the secondary separatrix, the magnetic axis, and the plasma boundary, respectively. The normalized flux is used as a proxy for the X-point separation distance, where $\psi_{N,2} = 1$ corresponds to an exact-SFD and increasing $\psi_{N,2}$ indicates larger X-point separation. The heat flux profiles for the large separation SFD-minus (green) are compared with the profiles from a UEDGE simulation that was developed for model validation purposes. As seen in Fig. 1(b), the predicted profiles from the analytical model are in excellent qualitative agreement with those computed using a simple physics model in UEDGE that assumed one-dimensional (flux-surface averaged) transport coefficients and a fixed carbon impurity fraction (more details of the UEDGE

simulation settings may be found in Section 4). We also note that for the large flux expansion SN equilibrium (red), the heat flux profile as computed by the simplified model resembles the well-known Eich divertor profile [39].

2.2. Particle flux and neutral pumping model

After calculating the perpendicular heat flux, we can immediately compute the particle flux profile on the divertor target as $\Gamma_{\perp}^{\mathrm{div}} = q_{\perp}^{\mathrm{div}}/\gamma T_e$ [40], where $\gamma = 7$ and $T_e \approx 50$ eV in the case of a fully-attached, sheath-limited divertor. To estimate the pumping performance for an equilibrium and given cryopump location, we employ the first-flight neutral transport model as described in [28], some details of which are presented here for completeness. First, the pump location is defined by the parameters R_{plen} and h_{plen}, the major radius of the pump plenum entrance and its height relative to the divertor target, respectively. A schematic of the pump inlet location is given in Fig. 1(a). The neutral flow rate I_0^{plen} into the pump inlet is then computed as [28],

$$I_0^{\mathrm{plen}} = 2\pi \int_{R_{\mathrm{min}}}^{R_{\mathrm{max}}} \Gamma_{\perp}^{\mathrm{div}}(R) F(R) T(R) R \, \mathrm{d}R, \tag{3}$$

where $F(R)$ is the geometric solid angle of the pump inlet at major radius R, $T(R)$ measures the probability that a neutral particle, originating at major radius R, will enter the pump before it is ionized, and the integral is taken over the radial extent of the particle flux profile from R_{min} to R_{max}. A required input to the calculation of the ionization probability is the divertor plasma density, which can be computed directly from the particle flux as $n = \Gamma_{\perp}^{\mathrm{div}}/\sin\theta_B\sqrt{2T_e/m_i}$ [40]. Furthermore, we assume for simplicity that all neutrals released from the divertor target surface are Franck–Condon neutrals with energy 3 eV. After computing the neutral flow rate into the pump, the pressure at the pump inlet can be computed directly as,

$$P_0^{\mathrm{plen}} \propto \frac{I_0^{\mathrm{plen}}}{T_n(S_{\mathrm{pump}} + C)}, \tag{4}$$

where S_{pump} is the volumetric pumping rate, C is the molecular conductance through the pump duct, and T_n is the neutral particle temperature. The expressions in (3) and (4) can therefore be used to determine the pump inlet pressure for a given equilibrium and pump entrance location using the divertor heat flux profile as computed in Section 2.1. This model is used in Section 3 to study the pumping characteristics of the equilibria contained within the SFD-minus database.

3. Optimal SFDs for power and particle exhaust

The simplified model was used to analyze a database of 70 SFD equilibria that were generated by a free-boundary Grad-Shafranov equilibrium solver. All equilibria in the database are SFD-minus configurations with X-point separation distances ranging from 8 to 24 cm ($\psi_{N,2} = 1.0006$ to $\psi_{N,2} = 1.0223$) and normalized flux at the $\lambda_q = 3$ mm surface of $\psi_{N,\lambda_q} = 1.015 \pm 0.008$. Furthermore, plasma pressure and current profiles were chosen to match scalar parameters $I_p = 2$ MA, $\beta_p = 1.0$, and $l_i = 0.6$. In this section, we present the results of the database analysis. In Section 3.1, the impact of variations in SFD magnetic topology on power partitioning and peak heat flux is assessed with the aim of identifying optimal divertor configurations for power handling. In Section 3.2, we analyze cryopump performance to determine pump locations that are compatible with a large assortment of SFD-minus equilibria.

3.1. Scaling of power exhaust with magnetic geometry

As discussed in Section 2, the power exhaust in the low-field-side SOL of the SFD-minus is partitioned between two activated strike points (SP2 and SP4) due to the presence of a secondary X-point in the SOL. It is therefore interesting to study the relative power flow to SP2 and SP4 as a function of parameters which define the divertor configuration. For this purpose, we introduce three SFD performance metrics, namely, the integrated power fraction $f_{\mathrm{SP}i}$ at strike point $i \in \{2, 4\}$, the peak perpendicular heat flux at each SP, and the heat flux reduction factor $\bar{q}_{\|i}$ for each SP. The integrated power fraction is defined as $f_{\mathrm{SP}i} = P_{\mathrm{SP}i}/(P_{\mathrm{SP2}} + P_{\mathrm{SP4}})$, where $P_{\mathrm{SP}i}$ is the total integrated power transported to SPi, while the peak heat flux at SPi is simply the maximum value of the perpendicular heat flux profile at SPi. Furthermore, we define the heat flux reduction factor $\bar{q}_{\|i} = q_{\|i}^{\mathrm{div,peak}}/q_{\|i}^{\mathrm{split,peak}}$, where $q_{\|i}^{\mathrm{div,peak}}$ is the peak parallel heat flux at SPi and $q_{\|i}^{\mathrm{split,peak}}$ is the peak parallel heat flux at the splitting front associated with SPi. Intuitively, $\bar{q}_{\|i}$ provides a measure of the diffusive spreading of the parallel heat flux which occurs as the SOL is traversed from the splitting front to SPi.

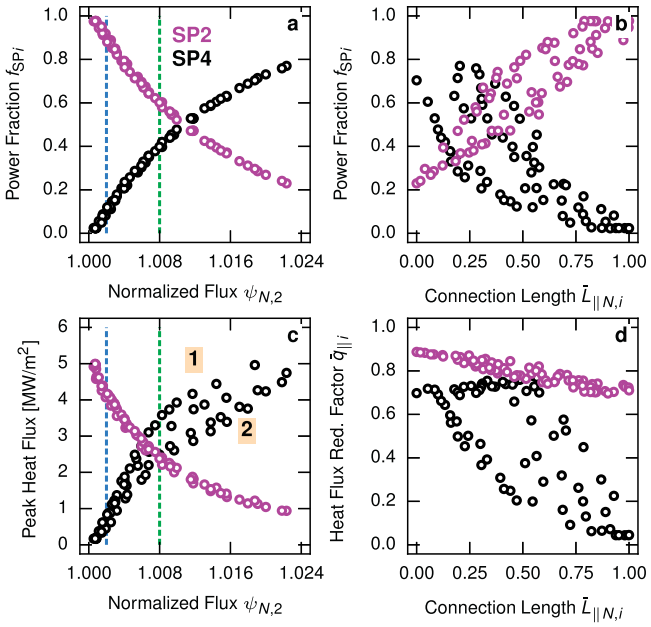

Fig. 2. Integrated power fraction (a,b), peak perpendicular heat flux (c), and heat flux reduction factor (d) at strike points SP2 (purple) and SP4 (black) in the SFD-minus as plotted against the normalized flux on the secondary separatrix $\psi_{N,2}$ (a,c) and the normalized connection length $\bar{L}_{\|N,i}$ (b,d), where $i \in \{2, 4\}$ denotes the strike point number. Also shown in (a,c) are green and blue dashed lines indicating the values of $\psi_{N,2}$ for the two similarly colored equilibria in Fig. 1. (For interpretation of the references to color in this figure legend, the reader is referred to the web version of this article.)

In Fig. 2, we plot the integrated power fraction, peak heat flux, and heat flux reduction factor at SP2 and SP4 for each of the equilibria in the SFD-minus database. As variables describing the SFD magnetic geometry, we choose the normalized flux on the secondary separatrix $\psi_{N,2}$ as well as the normalized connection length $\bar{L}_{\|N,i}$. To compute the normalized connection length, we first define $\bar{L}_{\|i} = L_{\|i}^{\mathrm{div}}/L_{\|i}^{\mathrm{tot}}$, where $L_{\|i}^{\mathrm{div}}$ is the parallel connection length from the splitting front to the divertor target and $L_{\|i}^{\mathrm{tot}}$ is the total connection length from the outer midplane to the target. Both $L_{\|i}^{\mathrm{div}}$ and $L_{\|i}^{\mathrm{tot}}$ are computed for the flux surface which is nearest to the corresponding separatrix on the low-field-side. The value of $\bar{L}_{\|N,i}$ at each strike point is then computed as $\bar{L}_{\|N,i} = (\bar{L}_{\|i} - \bar{L}_{\|i}^{\mathrm{min}})/(\bar{L}_{\|i}^{\mathrm{max}} - \bar{L}_{\|i}^{\mathrm{min}})$, where $\bar{L}_{\|i}^{\mathrm{min}}$ and $\bar{L}_{\|i}^{\mathrm{max}}$ are the minimum and maximum database values of $\bar{L}_{\|i}$ at SPi, respectively.

It is observed in Fig. 2(a) and (c) that there exists a strong correlation between the normalized flux $\psi_{N,2}$ and both the integrated power fraction and peak heat flux. A normalized flux $\psi_{N,2} \approx 1.011$ is required for an equal partitioning of the total power between SP2 and SP4, while the peak heat fluxes at SP2 and SP4 are equivalent for $\psi_{N,2} \approx 1.007$ (indicating that the optimal configuration for equal partitioning of the peak heat flux may resemble the equilibrium with green separatrices in

Fig. 1). We note that these trends agree quite well with those described in recent numerical studies of the SFD on TCV [41]. Discrepancies between the results of this paper and those of [41] are likely due to the use of different cross-field transport coefficients. We also note that the peak heat flux bifurcates into two branches for $\psi_{N,2} > 1.008$ due to fieldline angle-of-incidence variations. Branch 1 contains equilibria for which SP4 is located on the angled portion of the limiter at $R \approx 0.4$m and $Z \approx -1.6$m, while branch 2 contains equilibria for which SP4 is located on the horizontal portion of the limiter.

Fig. 2(b) and (d) illustrate that there also exists a correlation, albeit not as pronounced as those associated with $\psi_{N,2}$, between the normalized connection length and both the power fraction and heat flux reduction factor. In particular, the reduction factor $\bar{q}_{\|2}$ for SP2 appears to vary inversely with $\bar{L}_{\|N,2}$. This relation has a simple physical interpretation if we recall that larger values $\bar{L}_{\|N,2}$ correspond to equilibria with a larger fraction of their total connection lengths located between the splitting front and the divertor target. It is therefore to be expected that $\bar{q}_{\|2}$ varies inversely with $\bar{L}_{\|N,2}$, as diffusive transport is higher in the SP2 divertor leg for equilibria with larger values of $\bar{L}_{\|N,2}$. From a practical standpoint, the importance of $\bar{L}_{\|N,i}$ is that this parameter affords an additional degree-of-freedom for modifying the power exhaust characteristics of a SFD-minus once the value of $\psi_{N,2}$ has been fixed.

3.2. Optimal pump location and pump performance

In addition to an analysis of power exhaust in the SFD-minus configuration, the impact of SFD magnetic topology on the performance of a divertor cryopumping system was studied using the particle flux and neutral transport model as described in Section 2.2. Under the assumption that the volumetric pumping rate of a liquid Helium cooled cryopump on NSTX–U will be roughly 24 kL/s [27], it is simple to show using (4) that the minimum pressure at the pump inlet for pumping 10 MW (20 Torr-L/s) of neutral beam-heating is $P_0^{\text{plen}} \approx 0.83$ mTorr. The simplified particle flux and pumping model was therefore used to explore the range of SFD-minus equilibria and pump inlet locations that are compatible with the required inlet pressure. For each equilibrium in the database, the inlet pressure was computed as the pump inlet location was scanned from $R_{\text{plen}} = 0.65$ m to $R_{\text{plen}} = 0.85$ m in 0.01 m increments. The inlet height was fixed at $h_{\text{plen}} = 2.5$ cm for all calculations.

In Fig. 3, we display the pump inlet pressure P_0^{plen} as a function of the inlet location R_{plen} for a variety of SFD equilibria from the database. The two thick curves with data markers correspond to the two SFD-minus equilibria from Fig. 1 with $\psi_{N,2} = 1.002$ (blue) and $\psi_{N,2} = 1.008$ (green). Pump pressure-inlet calculations for several additional equilibria with $1.0008 \leq \psi_{N,2} \leq 1.0223$ are depicted in Fig. 3 as transparent curves. Higher inlet pressures are generally achieved across the range of locations for equilibria with smaller $\psi_{N,2}$. This result is consistent with physical intuition, as a larger fraction of the SOL exhaust in equilibria with smaller $\psi_{N,2}$ is deposited at SP2 near the pump entrance (as is depicted in Fig. 1). For instance, the equilibrium with $\psi_{N,2} = 1.002$ (blue) yields excellent pumping with a maximum pressure $P_0^{\text{plen}} \approx 1.7$ mTorr when $R_{\text{plen}} \approx 0.74$ m. Furthermore, the inlet pressure exceeds the 0.83 mTorr threshold of sufficient pressure throughout a 9 cm range of locations. We also observe that the inlet pressure for the equilibrium with $\psi_{N,2} = 1.008$ (green), while lower at most pump locations than the pressure when $\psi_{N,2} = 1.002$, still exceeds 0.83 mTorr across a 6 cm range of pump locations. It was determined that the optimal pump location $R_{\text{plen}} = 0.73$ m since the maximum percentage (77%) of the equilibria in the database have an inlet pressure in excess of 0.83 mTorr at this position. Pump placement at this location is advantageous as the large number of compatible equilibria relaxes the precision required of real-time SFD control systems. Furthermore, optimal placement is crucial for achieving acceptable simultaneous control of both power and particle exhaust. For instance, while the pump

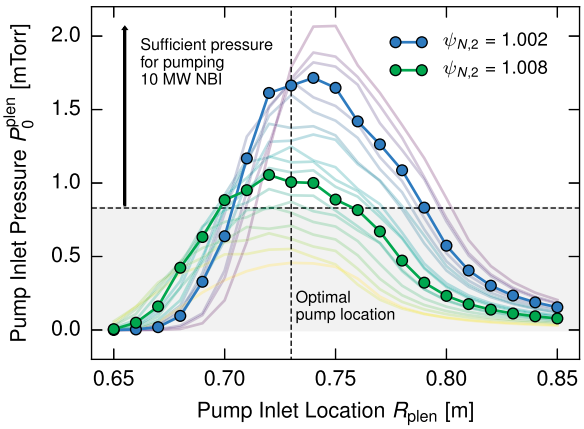

Fig. 3. Cryopump inlet pressure versus major radius of the pump inlet for the two SFD-minus equilibria shown in Fig. 1 with $\psi_{N,2} = 1.002$ (blue) and $\psi_{N,2} = 1.008$ (green), respectively. The horizontal black dashed line indicates the minimum inlet pressure of 0.83 mTorr that is required for pumping 10 MW neutral beam injection (NBI) using a cryopump with volumetric pumping rate of 24 kL/s. The vertical black dashed line indicates the optimal location of the cryopump inlet at which the maximum percentage (77%) of equilibria in the SFD database have an inlet pressure exceeding the minimum required value. Also shown as transparent curves are pump pressure-inlet calculations for several additional equilibria with $1.0008 \leq \psi_{N,2} \leq 1.0223$, where the colors from purple to yellow correspond to equilibria with increasing $\psi_{N,2}$. (For interpretation of the references to color in this figure legend, the reader is referred to the web version of this article.)

performance in a configuration with $\psi_{N,2} = 1.002$ is likely to be higher than that achieved when $\psi_{N,2} = 1.008$, the peak heat flux at SP2 (near the pump inlet), as seen in Fig. 1, is roughly twice as high when $\psi_{N,2} = 1.002$ than when $\psi_{N,2} = 1.008$. Based upon the predictions of the simple model, therefore, a SFD resembling the one in Fig. 1 for which $\psi_{N,2} = 1.008$ (green) may be a more attractive solution from a holistic standpoint due to the combination of excellent heat flux mitigation and sufficient pumping.

4. SFD simulations with UEDGE

A SFD-minus with X-point separation distance of 8.6 cm ($\psi_{N,2} = 1.0008$) – a configuration which is predicted by the simplified model to enable excellent neutral pumping – was selected from the equilibria database for further analysis with UEDGE. A computational grid for the equilibrium was created using Gingred, a state-of-the-art grid generator that was recently developed to enable grid generation for magnetic equilibria with multiple X-points such as the SFD [37]. The resulting grid spanned the range of normalized flux from $\psi_N = 0.80$ at the core-edge interface (CEI) to $\psi_N = 1.05$ in the far SOL. The grid geometry in the divertor region is shown in Fig. 4. We note that the computational grid extends beyond the target location for the cryopump entrance as computed in Section 3.

The UEDGE simulation settings that were used in this work were inherited primarily from previous simulation studies of the SFD [36]. In all simulations, the power entering the SOL was 5 MW and was partitioned evenly between the ion and electron fluids. Plasma density n_{core} at the CEI was constant during a given simulation but was varied between simulations, as is discussed in more detail below. Furthermore, neutral gas was injected at the high-field-side midplane with a Gaussian profile and rates ranging from 6.25×10^{20} s^{-1} to 1.56×10^{21} s^{-1} in the no-pumping case and from 2.34×10^{21} s^{-1} to 5.94×10^{21} s^{-1} in the pumping case. In each simulation, the gas injection rate was varied to ensure a constant 4 MW particle flow across the CEI from neutral beam injection. The cross-field particle diffusivity D varied from 0.1 m^{2}s^{-1} at the CEI to 1.5 m^{2}s^{-1} in the SOL. The cross-field thermal

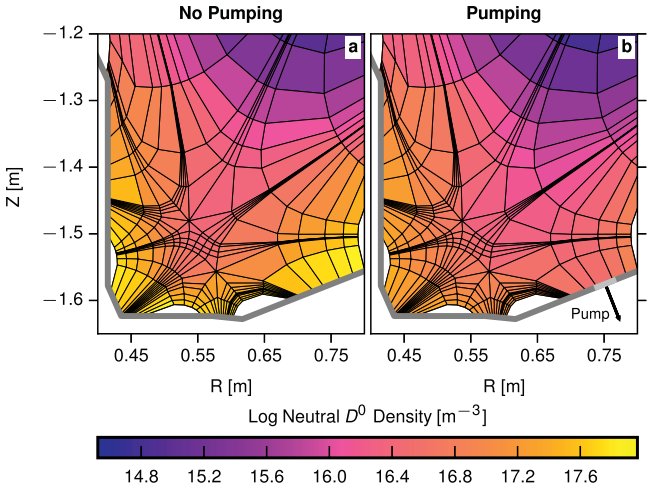

Fig. 4. Illustration of the SFD-minus grid that was generated for use in UEDGE. Plotted in color are two-dimensional contours of the neutral deuterium D^0 particle density in the case of (a) no pumping and (b) simulated cryopumping. Also shown in (b) is the grid cell boundary (with arrow protruding) which was used to simulate neutral particle removal with the cryopump.

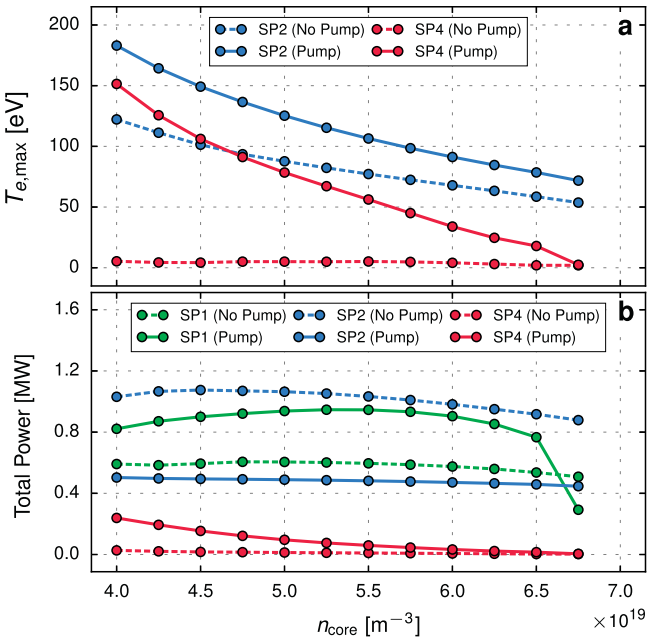

Fig. 5. Subset of UEDGE simulation results, namely (a) the maximum electron temperature $T_{e,max}$ at strike points SP2 (blue) and SP4 (red) and (b) the total power to each of the activated strike points, SP1 (green), SP2 (blue), and SP4 (red), as the core deuterium ion density n_{core} was scanned from 4×10^{19} m^{-3} to 6.75×10^{19} m^{-3} in increments of 0.25×10^{19} m^{-3}. At each value of core ion density, a simulation with (solid lines) and without (dashed lines) was performed. (For interpretation of the references to color in this figure legend, the reader is referred to the web version of this article.)

diffusivities for ions χ_i and electrons χ_e ranged from 1.5 m^2s^{-1} at the CEI for both species to 5.0 m^2s^{-1} in the SOL for ions and 6.0 m^2s^{-1} in the SOL for electrons, all of which are consistent with NSTX transport coefficients. All diffusivities were poloidally uniform.

Carbon impurity content was fixed at 3% of deuterium density for all simulations, while the recycling coefficient at the divertor targets was chosen to be 99% for ions to mimic high-recycling regimes relevant for NSTX. Neutral particle removal using a divertor cryopump was simulated by reducing the neutral albedo on the boundary of the grid cell that was nearest to the desired location of the pump entrance, as is shown in Fig. 4(b) (gray line segment and arrow). For the pumping case, neutral albedo was equal to 0.9 such that 10% of the neutral particles incident on the grid boundary were removed from the domain. For the no-pumping case, neutral albedo was equal to 1.0. We see in Fig. 4(b) that the neutral albedo reduction results in an order-of-magnitude decrease in the neutral deuterium density relative to the no-pumping case in the region near the pumping grid cell.

A series of simulations was performed in which the core deuterium ion density n_{core} was scanned from 4×10^{19} m^{-3} to 6.75×10^{19} m^{-3} in increments of 0.25×10^{19} m^{-3}. At each value of core ion density, UEDGE simulations with and without the neutral pumping boundary condition (reduced neutral albedo) were performed. In Fig. 5, we provide a subset of results from the simulations with and without pumping, namely (a) the maximum electron temperature $T_{e,max}$ at SP2 and SP4 in the low-field-side SOL and (b) the total power to each of the activated strike points, SP1, SP2, and SP4. We emphasize that the goal of this work is to identify qualitative changes in SOL properties such as electron temperature, neutral density, and power flux that result from variations in core ion density and the rate of neutral particle removal near the outer strike point. Numerical values should only be considered in a relative sense as no efforts were made to match experimentally-observed values. Indeed, there is currently no available NSTX–U experimental data for discharges with either a SFD or cryopumping system.

As seen in Fig. 5(a), a significant increase in the maximum electron temperature at each SP is observed across the range of core densities when the pumping boundary condition is enabled. At SP2, the $T_{e,max}$ increase due to pumping is largest at low core density. The rise in $T_{e,max}$ at SP2, which is accompanied by a corresponding increase in the maximum ion temperature (not shown), is likely the result of a decrease in the rate of collisional energy transfer due to the reduced neutral particle density along the divertor target resulting from the pumping boundary condition. The increase in $T_{e,max}$ at SP2 is accompanied by a corresponding increase in the maximum electron temperature at SP4 for each value of core density. In the case of no-pumping, SP4 is fully-detached at all values of n_{core} with $T_{e,max} < 10$ eV. The electron temperature rise at SP2 and SP4 is less pronounced at higher values of core density. However, we see that, with the pumping boundary condition enabled, SP4 does not achieve detachment until $n_{core} = 6.75 \times 10^{19}$ m^{-3}. We note that SP2 does not detach at any combination of core density and pumping condition in this simplified UEDGE model.

Fig. 5(b) displays the total power to each of the activated strike points, SP1, SP2, and SP4, as a function of core ion density and pumping boundary condition. (SP3 is disconnected from the outer SOL and therefore receives minimal power, an observation which is consistent with the predictions of the simplified power flux model presented in Section 2.) We note that, in all simulations described in this work, roughly 60% of the power entering the SOL exits the computational domain toward the walls and is therefore not transported to one of the activated SPs. This power loss to the walls has always been observed in UEDGE simulations. As seen in Fig. 5(b), a significant redistribution of power to the SPs occurs when the pumping boundary condition is enabled. In the no-pumping case, nearly all SOL power is split between outer SP2 and inner SP1, with SP2 receiving between 0.9 MW and 1.1 MW and SP1 receiving between 0.5 MW and 0.6 MW across the range of core densities. In the pumping case, however, a significant fraction of SOL power is diverted away from SP2 toward SP1 and SP4 with SP1 receiving the majority of total power at almost all values of core density (the drop in power to the inner target at $n_{core} = 6.75 \times 10^{19}$ m^{-3} is due to the onset of detachment at SP1). When the pumping boundary condition is enabled, SP4 also receives an appreciable fraction of SOL power until the strike point detaches at larger core densities. A consequence of this power redistribution is that the ideal SFD for equal partitioning of the peak perpendicular heat flux between SP2 and SP4 is likely to vary somewhat from the configuration

identified by the simple analytical model due to the pumping-induced reduction of power at SP2.

5. Conclusion

A simple analytical model and simulations performed with UEDGE were used to identify optimal SFD configurations for heat flux mitigation and cryopumping performance on NSTX–U. A model was presented that describes the partitioning of power and particle exhaust in the SFD as a result of diffusive transport to multiple activated SPs. The model was then used to analyze a database of 70 SFD-minus equilibria. It was shown that the normalized flux on the secondary separatrix $\psi_{N,2}$ and the normalized connection length $\bar{L}_{\|N}$ are two parameters which may be used to modify the power exhaust characteristics of the SFD-minus. Furthermore, the optimal position for the entrance to a divertor cyropump on NSTX–U was determined to enable acceptable pumping in a variety of SFD equilibria. Pump placement at the optimal location is advantageous as the large number of compatible equilibria relaxes the precision required of real-time SFD control systems. UEDGE simulations indicated that a significant redistribution of power to the SPs occurs as a result of neutral particle pumping. The simulations suggest that the ideal SFD-minus equilibria for power exhaust and pumping may vary somewhat from those identified with the simple model when self-consistent transport physics is considered. In particular, the optimal SFD-minus for equal power partitioning between SP2 and SP4 may actually require a power fraction $f_{SP2} \approx 0.9$ (similar to the blue equilibrium in Fig. 1) as calculated by the simple model to compensate for the power redistribution that occurs due to pumping.

Further work is required to fully-investigate the compatibility of the SFD configuration with a cryopumping system on NSTX–U. For instance, the simplified analytical model of Section 2 should be extended to analyze a much larger variety of pump inlet geometries than the idealized configurations which were considered in this paper. Promising pump configurations should also be studied using kinetic codes such as EIRENE to account for molecular phenomena that are beyond the scope of both the simplified model and UEDGE. The results of this work also suggest future avenues for the development of real-time systems for SFD configuration control and heat flux mitigation. As one example, simple modeling of SFD power exhaust may facilitate improvements in real-time equilibrium reconstruction methods for advanced divertors by allowing for estimates of the magnetic configuration to be obtained from real-time divertor heat flux measurements.

Conflict of interest

The authors declare that they have no known competing financial interests or personal relationships that could have appeared to influence the work reported in this paper.

Acknowledgments

This research was supported by the United States Department of Energy (DoE) under contract number DE-AC02-09CH11466.

Notes: The digital data for this publication can be found in: https://dataspace.princeton.edu/jspui/handle/88435/dsp01j6731612k.

Notice: This manuscript is based upon work supported by the United States Department of Energy, Office of Science, Office of Fusion Energy Sciences, and has been authored by Princeton University under contract number DE-AC02-09CH11466 with the United States Department of Energy. The publisher, by accepting the article for publication, acknowledges that the United States Government retains a non-exclusive, paid-up, irrevocable, world-wide license to publish or reproduce the published form of this manuscript, or allow others to do so, for United States Government purposes.

Supplementary material

Supplementary material associated with this article can be found, in the online version, at 10.1016/j.nme.2019.03.003

References

[1] J.E. Menard, S. Gerhardt, M. Bell, et al., Overview of the physics and engineering design of NSTX upgrade, Nucl. Fusion 52 (2012), https://doi.org/10.1088/0029-5515/52/8/083015.
[2] J.E. Menard, J.P. Allain, D.J. Battaglia, Overview of NSTX Upgrade initial results and modelling highlights, Nucl. Fusion 57 (2017), https://doi.org/10.1088/1741-4326/aa600a.
[3] D.J. Battaglia, M.D. Boyer, S. Gerhardt, et al., Scenario development during commissioning operations on the National Spherical Torus Experiment Upgrade, Nucl. Fusion 58 (2018), https://doi.org/10.1088/1741-4326/aaa6e0.
[4] M. Ono, S.M. Kaye, Y.-K. Peng, et al., Exploration of spherical torus physics in the NSTX device, Nucl. Fusion 40 (2000), https://doi.org/10.1088/0029-5515/40/3Y/316.
[5] A. Sykes, R.J. Akers, L.C. Appel, et al., First results from MAST, Nucl. Fusion 41 (2001), https://doi.org/10.1088/0029-5515/41/10/310.
[6] S.M. Kaye, R.E. Bell, D. Gates, et al., Scaling of Electron and Ion Transport in the High-Power Spherical Torus NSTX, Phys. Rev. Lett. 98 (2007), https://doi.org/10.1103/PhysRevLett.98.175002.
[7] M. Podestà, W.W. Heidbrink, D. Liu, et al., Experimental studies on fast-ion transport by Alfvén wave avalanches on the National Spherical Torus Experiment, Phys Plasmas 16 (2009), https://doi.org/10.1063/1.3080724.
[8] S.P. Gerhardt, D.A. Gates, S.M. Kaye, et al., Recent progress towards an advanced spherical torus operating point in NSTX, Nucl. Fusion 51 (2011), https://doi.org/10.1088/0029-5515/51/7/073031.
[9] M. Greenwald, Density limits in toroidal plasmas, Plasma Phys. Control. Fusion 44 (2002), https://doi.org/10.1088/0741-3335/44/8/201.
[10] T.K. Gray, R. Maingi, V.A. Soukhanovskii, et al., Dependence of divertor heat flux widths on heating power, flux expansion, and plasma current in the NSTX, J. Nucl. Mater. 415 (2011), https://doi.org/10.1016/j.jnucmat.2011.01.029.
[11] D.D. Ryutov, Geometrical properties of a "snowflake" divertor, Phys Plasmas 14 (2007), https://doi.org/10.1063/1.2738399.
[12] F. Piras, S. Coda, B.P. Duval, et al., Snowflake divertor experiments on TCV, Nucl. Fusion 52 (2010), https://doi.org/10.1088/0741-3335/52/12/124010.
[13] H. Reimerdes, G.P. Canal, B.P. Duval, et al., Power distribution in the snowflake divertor in TCV, Plasma Phys. Control. Fusion 55 (2013), https://doi.org/10.1088/0741-3335/55/12/124027.
[14] W.A.J. Vijvers, G.P. Canal, B. Labit, et al., Power exhaust in the snowflake divertor for L- and H-mode TCV tokamak plasmas, Nucl. Fusion 54 (2014), https://doi.org/10.1088/0029-5515/54/2/023009.
[15] G.P. Canal, T. Lunt, H. Reimerdes, et al., Enhanced ExB drift effects in the TCV snowflake divertor, Nucl. Fusion 55 (2015), https://doi.org/10.1088/0029-5515/55/12/123023.
[16] B. Labit, G.P. Canal, N. Christen, et al., Experimental studies of the snowflake divertor in TCV, Nuclear Mater. Energy 12 (2017), https://doi.org/10.1016/j.nme.2017.03.013.
[17] V.A. Soukhanovskii, S.L. Allen, M.E. Fenstermacher, et al., Developing physics basis for the snowflake divertor in the DIII-D tokamak, Nucl. Fusion 58 (2018), https://doi.org/10.1088/1741-4326/aaa6de.
[18] G. Calabrò, B.J. Xiao, S.L. Chen, et al., EAST alternative magnetic configurations: modelling and first experiments, Nucl. Fusion 55 (2015), https://doi.org/10.1088/0029-5515/55/8/083005.
[19] V.A. Soukhanovskii, J.-W. Ahn, R.E. Bell, et al., Taming the plasma-material interface with the 'snowflake' divertor in NSTX, Nucl. Fusion 51 (2011), https://doi.org/10.1088/0029-5515/51/1/012001.
[20] V.A. Soukhanovskii, R.E. Bell, A. Diallo, et al., Snowflake divertor configuration studies in National Spherical Torus Experiment, Phys Plasmas 19 (2012), https://doi.org/10.1063/1.4737117.
[21] V.A. Soukhanovskii, S.L. Allen, M.E. Fenstermacher, et al., Snowflake Divertor Experiments in the DIII-D, NSTX, and NSTX-U Tokamaks Aimed at the Development of the Divertor Power Exhaust Solution, IEEE Trans. Plasma Sci. 44 (2016), https://doi.org/10.1109/TPS.2016.2625325.
[22] T.D. Rognlien, J.L. Milovich, M.E. Rensink, G.D. Porter, A fully implicit, time dependent 2-D fluid code for modeling tokamak edge plasmas, J. Nucl. Mater. 196–198 (1992), https://doi.org/10.1016/S0022-3115(06)80058-9.
[23] E.T. Meier, V.A. Soukhanovskii, S. Gerhardt, J.E. Menard, T.D. Rognlien, Multi-Fluid Transport Modeling of NSTX Upgrade Standard and Snowflake Divertor Configurations, Contrib. Plasma Phys. 54 (2014), https://doi.org/10.1002/ctpp.201410055.
[24] E.T. Meier, S. Gerhardt, J.E. Menard, T.D. Rognlien, V.A. Soukhanovskii, Modeling divertor concepts for spherical tokamaks NSTX-U and ST-FNSF, Nucl. Fusion 55 (2015), https://doi.org/10.1088/0029-5515/55/8/086002.
[25] M.M. Menon, P.M. Anderson, C.B. Baxi, et al., Particle Exhaust Scheme Using an In-Vessel Cryocondensation Pump in the Advanced Divertor Configuration of the DIII-D Tokamak, Fusion Sci. Technol. 22 (1992), https://doi.org/10.13182/FST92-A30095.
[26] B. Streibl, S. Deschka, O. Gruber, et al., In-Vessel Cryo Pump For ASDEX Upgrade Divertor II, Proceedings of the 19th Symposium on Fusion Technology, (1996). Lisbon, Portugal

[27] J.M. Canik, R. Maingi, S.P. Gerhardt, et al., Physics design of a cryo-pumping system for NSTX–U, Proceedings of the 54th Annual Meeting of the APS Division of Plasma Physics, (2012). Providence, RI
[28] R. Maingi, J.G. Watkins, M.A. Mahdavi, L.W. Owen, Pump plenum pressure dependence on divertor plasma parameters and magnetic geometry in the DIII-D tokamak, Nucl. Fusion 39 (1999), https://doi.org/10.1088/0029-5515/39/9/311.
[29] D. Reiter, C. May, D. Coster, R. Schneider, Time dependent neutral gas transport in tokamak edge plasmas, J. Nucl. Mater. 220–222 (1995), https://doi.org/10.1016/0022-3115(94)00648-2.
[30] R. Schneider, X. Bonnin, K. Borrass, et al., Plasma Edge Physics with B2-Eirene, Contrib. Plasma Phys. 46 (2006), https://doi.org/10.1002/ctpp.200610001.
[31] F. Wagner, A study of the perpendicular particle transport properties in the scrape-off layer of ASDEX, Nucl. Fusion 25 (1985), https://doi.org/10.1088/0029-5515/25/5/002.
[32] E. Kolemen, P.J. Vail, M.A. Makowski, et al., Initial development of the DIII-D snowflake divertor control, Nucl. Fusion 58 (2018), https://doi.org/10.1088/1741-4326/aab0d3.
[33] P.J. Vail, M.D. Boyer, A.S. Welander, E. Kolemen, Design and simulation of the snowflake divertor control for NSTX-U, Plasma Phys. Control. Fusion 61 (2019), https://doi.org/10.1088/1361-6587/aaf94a.
[34] T. Lunt, H. Zohm, A. Herrmann, et al., Proposal of an alternative upper divertor in ASDEX Upgrade supported by EMC3-EIRENE simulations, Nuclear Mater. Energy 12 (2017), https://doi.org/10.1016/j.nme.2016.12.035.
[35] T. Lunt, G.P. Canal, Y. Feng, et al., First EMC3-Eirene simulations of the TCV snowflake divertor, Plasma Phys. Control. Fusion 56 (2014), https://doi.org/10.1088/0741-3335/56/3/035009.
[36] O. Izacard, F. Scotti, V. Soukhanovksii, et al., UEDGE modeling of snowflake divertors in NSTX-U, Proceedings of the 58th Annual Meeting of the APS Division of Plasma Physics, (2016). San Jose, CA
[37] O. Izacard, M. Umansky, Gingred, a General Grid Generator for 2D Edge Plasma Modeling, 2017.
[38] O. Pan, T. Lunt, M. Wischmeier, D. Coster, The ASDEX Upgrade team, SOLPS simulations of detachment in a snowflake configuration for the future upper divertor in ASDEX Upgrade, Plasma Phys. Control. Fusion 60 (2018), https://doi.org/10.1088/1361-6587/aac706.
[39] T. Eich, A.W. Leonard, R.A. Pitts, et al., Scaling of the tokamak near the scrape-off layer H-mode power width and implications for ITER, Nucl. Fusion 53 (2013), https://doi.org/10.1088/0029-5515/53/9/093031.
[40] P.C. Stangeby, The Plasma Boundary of Magnetic Fusion Devices, first ed., Institute of Physics Publishing, Bristol, 2000.
[41] T. Lunt, G.P. Canal, B.P. Duval, et al., Numerical study of potential heat flux mitigation effects in the TCV snowflake divertor, Plasma Phys. Control. Fusion 58 (2016), https://doi.org/10.1088/0741-3335/58/4/045027.